

# The Devil is in the Details: Compact Structures in Pulsar Wind Nebulae

Patrick Slane

*Harvard-Smithsonian Center for Astrophysics  
60 Garden Street, Cambridge, MA 02138, USA*

---

## Abstract

The large-scale structure of pulsar wind nebulae (PWNe) tells us a considerable amount about their average magnetic fields, the total particle input from the pulsar winds, and the confining pressure at their outer boundaries. However, the details of the pulsar outflow, the sites of shocks and particle acceleration, the effects of instabilities in the magnetic field, and the interaction between the relativistic wind and the surrounding ejecta are contained in small-scale structures, where we observe jets and toroidal structures, time-varying emission from compact clumps, and filaments in both the inner and outer regions of the nebulae. Here I review recent observational studies of compact structures in PWNe and present current scenarios (and questions) regarding their origin.

*Key words:* ISM: general, stars: neutron, stars: winds, outflows

---

## 1 Introduction

Our basic understanding of PWNe stems from the picture presented by Rees and Gunn (1974), and expanded upon by Kennel and Coroniti (1984), in which an energetic axisymmetric wind is injected from a pulsar into its surroundings. As illustrated schematically in Figure 1, the structure of a PWN is regulated by the input power from the pulsar and the density of the medium into which the nebula expands; the pulsar wind and wound-up toroidal magnetic field inflates a bubble which is confined in the outer regions by the expanding shell of ejecta or interstellar material swept up by the SNR blast wave. The boundary condition established by the expansion at the nebula radius  $r_N$  results in the formation of a wind termination shock at which the highly relativistic pulsar wind is decelerated to merge with the particle flow in the nebula. The shock

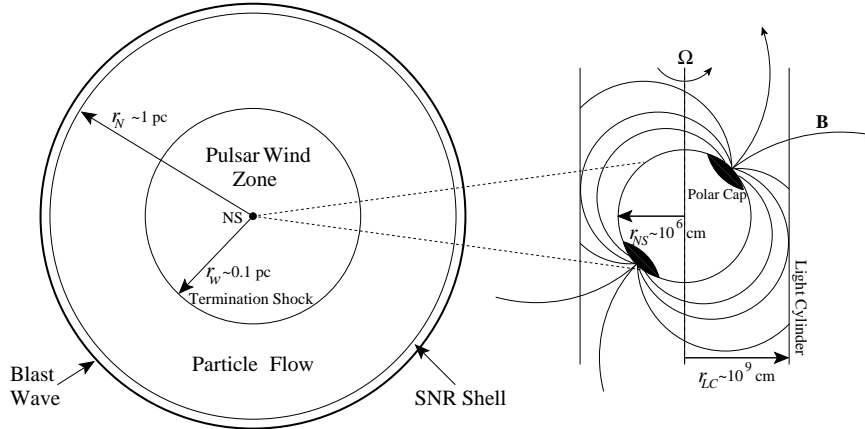


Fig. 1. Schematic view of a pulsar and its wind nebula. See the text for a complete description. (Note the logarithmic size scaling in the PWN figure when comparing with images shown elsewhere in the text.)

forms at the radius  $r_w$  at which the ram pressure of the wind is balanced by the internal pressure of the PWN:

$$r_w = \sqrt{\dot{E}/(4\pi\eta cp)}, \quad (1)$$

where  $\dot{E}$  is the rate at which the pulsar injects energy into the wind,  $\eta$  is the fraction of a spherical surface covered by the wind, and  $p$  is the total pressure outside the shock. Ultimately, the pressure in the nebula is believed to reach the equipartition value; a reasonable pressure estimate can be obtained by integrating the broad-band spectrum of the nebula, using standard synchrotron emission expressions, and assuming equipartition between particles and the magnetic field. Typical values yield termination shock radii of order 0.1 pc, which yields an angular size of several arcsec at distances of a few kpc.

As the relativistic fluid comprising the PWN encounters the freely-expanding ejecta, Rayleigh-Taylor instabilities result in the formation of a network of dense, optical line-emitting filaments (Jun, 1998). The density and magnetic field strength become enhanced in regions where the PWN creates these filaments, producing enhanced synchrotron emission observed as radio filaments. Due to the pinching effect of the global toroidal magnetic field, the overall morphology of a young PWN is often elongated along the pulsar spin axis (Begelman & Li, 1992; van der Swaluw et al., 2004). Along the rotation axis the flow becomes collimated, producing jets. Pinch instabilities may disrupt the toroidal structure, however, changing the structure of the magnetic field in the outer nebula regions and relaxing the collimation of the jets far from the pulsar (Begelman, 1998).

The overall geometry of the PWN, as well as that of the emission from jets or ring-like structures near the termination shock, thus provides a direct in-

dication of the pulsar geometry. The details of the jet morphology and the emission structure in the postshock region provide the strongest constraints available on wind composition and particle acceleration in PWNe. For cases in which the pulsar proper motion is also known, constraints on the kick velocity mechanism can be derived based on the degree of alignment between the velocity vector and the pulsar spin axis.

## 2 Pulsar Jets and Tori

In the inner portions of the Crab Nebula, optical wisps mark the position of the wind termination shock, at a distance of  $\sim 0.1$  pc from the pulsar. The brightness and position of these wisps varies in time, with inferred outflow speeds up to  $0.7c$  (Hester, 1998). As shown in Figure 2 (left), high resolution X-ray images reveal a ring of emission at the position of the wisps (Weisskopf et al., 2000), providing a direct connection between the unshocked pulsar wind and the bulk properties of the nebula. Material from the inner ring forms a series of toroidal X-ray wisps that are variable with time (Hester et al., 2002). The geometry of these X-ray features imply a tilted torus, and a jet of material flows perpendicular to the plane of the toroid, extending some 0.25 pc from the pulsar. A faint counterjet is also observed, along with significantly enhanced X-ray emission from the leading portion of the toroid. Both effects presumably result from Doppler beaming of the outflowing material, whereby the X-ray intensity varies with viewing angle:

$$\frac{I}{I_0} = \left[ \frac{\sqrt{1 - \beta^2}}{1 - \beta \cos \theta} \right]^{\alpha+1} \quad (2)$$

where  $\beta = v/c$  is the flow speed,  $\alpha$  is the photon index of the synchrotron spectrum, and  $\theta$  is the angle of photon propagation relative to the flow direction (Pelling et al. , 1987). One troubling aspect of this suggestion is that the brightness distribution around the inner ring does not match that of the outer toroid; indeed, the brightness is rather uniform except for some small clump-like structures that vary in position and brightness with time (see Section 3).

The process by which particles are accelerated from  $\gamma \sim 10^4$ , as expected in the wind outside the pulsar light cylinder, to the  $\gamma > 10^6$  required to explain the emission of synchrotron X-rays (assuming a magnetic field of  $\sim 300\mu\text{G}$ ), is not understood. Moreover, the production of radio-emitting electrons is not even predicted by the model of Kennel and Coroniti (1984). Yet recent VLA observations show variable structures very similar to the optical wisps, indicating that acceleration of the associated particles must be occurring in

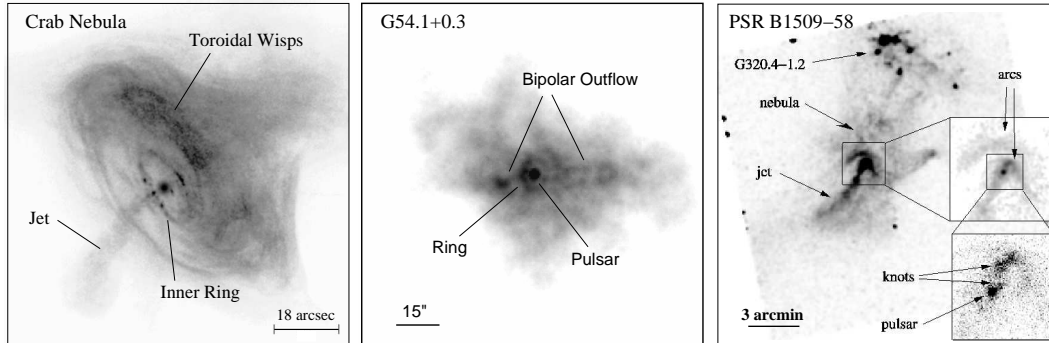


Fig. 2. *Chandra* images of the Crab Nebula (left), G54.1+0.3 (center), and PSR B1509–58 (right) showing the complex emission from these PWNe, including jet outflows and toroidal structures.

the same region as for the X-ray-emitting particles (Bietenholz et al., 2004).

A handful of other PWNe display X-ray features that suggest the presence of extended ring-like structures and narrow collimated components. The size of the ring-like features (or, in some cases, the slight extent of the compact source) places the emission region near the pulsar wind termination shock. The spectral and temporal properties of the collimated structures argue that they are focused jets of high speed material, as observed in the Crab. Such observations have already begun to inspire new axisymmetric MHD models that predict similar features (e.g., Komissarov & Lyubarsky 2004), and ongoing observational studies promise to further constrain and refine such models. In particular, the confining mechanism for jets is not well-understood; many jets display some amount of curvature, with the Vela pulsar jet being an extreme example in which the morphology is observed to change on timescales of months (Pavlov et al., 2003). This may be the result of pinch instabilities disrupting the toroidal structure of the confining magnetic field (Begelman 1998), or could be indicative of an interaction of the jet material with the ambient medium. There also appears to be a wide variation in the fraction of spin-down energy channeled into the jets, ranging from roughly  $2.5 \times 10^{-5}$  for PSR J0205+6449 in 3C 58 to nearly  $10^{-3}$  for PSR B1509–58 based upon their synchrotron spectra (Slane et al. 2004, Gaensler et al. 2002). And, while Doppler beaming is invoked to explain the large brightness variations in jets and the associated counterjets, as well as around the observed toroidal structures, it is not clear that this alone is sufficient to explain the observed jet/counterjet brightness ratios. The nature of the curved and time-variable wisps outside the termination shock remains in question as well (see Section 3).

*Chandra* observations of G54.1+0.3 (Lu et al., 2002) reveal a central 136 ms pulsar (Camilo et al., 2002) embedded in a diffuse  $1'5 \times 1'2$  ( $2.2 \text{ pc} \times 1.8 \text{ pc}$ ) nebula, assuming a distance of 5 kpc (Figure 2, center). The radio luminosity is among the lowest of the known young pulsars, although pulsations at the

radio period are clearly seen in X-rays as well. The pulsar is surrounded by a  $5''.7 \times 3''.7$  ( $0.14 \text{ pc} \times 0.09 \text{ pc}$ ) X-ray ring, with the long axis oriented roughly north-south, suggesting an inclination angle of about  $40^\circ$ . The X-ray emission is brightest along the eastern limb, and when interpreted as the result of Doppler boosting, implies a post-shock velocity of  $\sim 0.6c$  (Lu et al. 2002; Romani & Ng 2003). The spectrum of the ring is well-described by a power law and is harder than that for the surrounding diffuse emission. It is thus similar in many respects to the X-ray torus in the Crab Nebula. However, it comprises only  $\sim 10\%$  of the extended emission in G54.1+0.3, while the torus in the Crab dominates the X-ray flux. The pulsar in G54.1+0.3 is also much less luminous than the Crab Pulsar.

The *Chandra* data also reveal faint bipolar elongations running roughly E-W, perpendicular to the long axis of the ring. The spectra from these regions are also harder than that of the diffuse nebula, suggesting lower synchrotron losses or more recent particle injection. These apparent outflows, which presumably lie along the pulsar rotation axis, are more diffuse than the jets in the Crab Nebula, yet appear to carry away a considerably larger fraction of the energy; they comprise roughly the same luminosity as the central ring, which is in stark contrast to the Crab where the torus outshines the jets by a large factor. The structure of the elongation in the east appears dominated by a clump of emission well-removed from the pulsar.

*Chandra* observations of PSR B1509–58 (Gaensler et al., 2002) demonstrate that this young and energetic pulsar associated with G320.4–1.2 powers an extended and extremely complicated PWN, with structures on scales from  $\sim 10'$  ( $\sim 15 \text{ pc}$  at the distance of 5.2 kpc) down to the spatial resolution limit (Figure 2, right). On the largest scales, the elongated PWN has a clear axis of symmetry centered on the pulsar, presumably representing the projected orientation of the pulsar spin axis. To the southeast of the pulsar, the nebula is dominated by a narrow jet-like feature approximately 6 pc in length, lying along this axis and displaying a distinctly harder spectrum than the average for the nebula. If this spectral difference is interpreted as a lack of synchrotron cooling in the former component, one infers a minimum flow speed in the jet-like component of  $v_f \gtrsim 0.2c$ ; the lack of a similar feature to the north can be explained by Doppler boosting for this speed of outflow if the pulsar’s spin axis is inclined to the line-of-sight by  $\lesssim 30^\circ$  (Gaensler et al., 2002).

In the central region of the PWN, a pair of semi-circular arcs lie  $\sim 0.5$  and  $\sim 1 \text{ pc}$  to the north of the pulsar. Gaensler et al. (2002) note that if the inner region of these arcs represents the position of the pulsar wind termination shock, then the flow time to the arcs is much shorter than the synchrotron lifetime of the emitting particles based on equipartition estimates of the magnetic field. Thus, unlike for the Crab torus, where these timescales are similar, the emission from the arcs is not the result of large synchrotron cooling at this

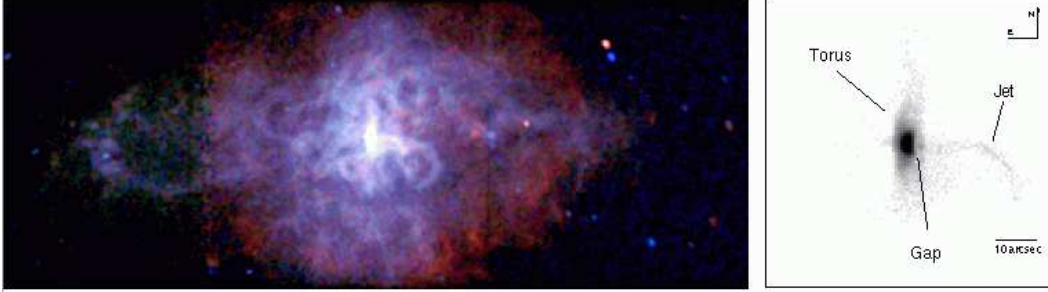


Fig. 3. Left: *Chandra* image of 3C 58. Colors correspond to the energy bands 0.5-1.0 keV (red), 1.0-1.5 keV (green), and 1.5-10 keV (blue). Complex filamentary loops fill the interior region, and a softening of the spectrum with radius is evidenced by the red outer regions – an effect resulting from both synchrotron aging of the electrons and the presence of a soft thermal shell. Right: The innermost region of 3C 58 showing the neutron star embedded in an elongated structure. A curved jet extends to the west, with a hint of a counterjet component in the east.

position. Instead, the arcs appear to resemble the series of concentric wisps seen for the Crab; if interpreted as sites of electron compression in an ion-dominated flow (as modeled for the Crab by Gallant & Arons, 1994), one can calculate an electron/positron termination shock radius of  $r_w \approx 0.5$  pc, and a nebular magnetic field of  $B_n \sim 8 \mu\text{G}$  (Gaensler et al., 2002).

The innermost region of 3C 58 (see Figure 3) consists of a bright, elongated compact structure centered on the pulsar J0205+6449. This inner nebulosity is bounded along the western edge by a radio wisp (Frail and Moffett, 1993), and is suggestive of a toroidal structure that is tilted about a north-south axis, with the pulsar at its center, and with a jet-like feature extending to the west. The eastern side of the toroid is slightly brighter than the western side, suggesting that the eastern side is beamed toward us. If interpreted as a circular termination shock zone, the inferred inclination angle in the plane of the sky is roughly 70 degrees (Slane et al., 2002). The luminosity of the toroidal region is  $L_x(0.5 - 10 \text{ keV}) = 5.3 \times 10^{33} \text{ erg s}^{-1}$ .

The elongated structure extending westward from the position of the pulsar has the appearance of a jet (Figure 3, right). Its orientation is consistent, in projection, with the pulsar rotation axis inferred from the wind termination shock region discussed above, and also the east-west elongation of the entire PWN. The structure shows considerable curvature, similar to that seen in the Crab Pulsar jet. The power law index of the jet spectrum does not vary along the length of the feature, indicating that, as for PSR B1509–58, the flow time across the jet is shorter than the synchrotron lifetime of the radiating particles. This sets a limit of  $v > 0.01c$  for the outflowing material assuming a minimum-energy magnetic field of  $\sim 35 \mu\text{G}$  (Slane et al., 2004). A faint structure that may be a counterjet is observed to the east of the pulsar. However, the jet/counterjet intensity ratio is  $> 5$  which, from Eq. 2, requires  $v > 0.8c$ ,

i.e., a supersonic flow. The observed luminosity is nearly a factor of 10 smaller than that for the torus. For the Crab Nebula, the torus is nearly 20 times more luminous than the jet in X-rays, while for PSR B1509–58 the jet is brighter than the extended inner emission (Gaensler et al. 2002).

The jet/torus morphology observed in these PWNe provides the geometry of the pulsar system, yielding both the projected direction of the spin axis and the inclination angle. Modeling of such emission in other PWNe holds promise for understanding the kicks that give pulsars their large space velocities (Ng and Romani, 2004). The jets observed in the Crab and Vela pulsars, for example, are aligned with their proper motion vectors (Aschenbach & Brinkman 1975; Helfand et al. 2001). If the kick that gave these pulsars their proper motion was generated in the supernova explosion by some asymmetric mass ejection, then this alignment requires an initial pulsar spin period that is short relative to the kick timescale, so that the impulse of the kick is averaged over many rotations of the star (Lai et al., 2001). Romani and Ng (2003) reach similar conclusions for PSR J0538+2817 in the supernova remnant S147. By modeling the faint extended PWN emission as a jet and torus, they derive a spin axis direction that is aligned with the vector from the SNR center to the current pulsar position. For some pulsars [e.g. J0205+6449 in 3C 58 (Murray et al., 2002) and J1811–1925 in G11.2–0.3 (Kaspi et al., 2001)], we believe that the initial spin period was relatively long  $> 50$  ms. If pulsar kicks are hydrodynamically-driven, where timescales of order 100 ms are expected (Lai et al., 2001), this would suggest that the proper motions of these pulsars should not necessarily be aligned with the jet direction. Future radio timing observations of these pulsars will ultimately lead to such proper motion measurements.

### 3 Time-Variable Structure in Pulsar Winds

Early optical studies of the Crab revealed dynamic changes in the inner part of the nebula (Scargle, 1969). Temporal variability in X-rays over long timescales was also revealed with ROSAT observations (Greiveldinger and Aschenbach, 1999). Using a series of HST observations with short sampling intervals, Hester (1998) showed that the Crab torus is comprised of a series of wisps that move outward at speeds of  $\sim 0.5c$ , and concluded that they result from unstable synchrotron cooling of magnetic flux tubes. An alternative view is that the wisps are structures formed by compression of the magnetic field and electron-positron pair plasma by magnetosonic waves produced by instabilities in ion gyration orbits, with the periodicity of the waves being associated with the ion Larmor time (Gallant & Arons 1994; Spitkovsky & Arons), a picture that appears to be more consistent with the structure of arcs observed around PSR B1509–58 as well (Gaensler et al., 2002). A series of joint HST and

Chandra observations of the Crab shows that these moving wisps are also observed in X-rays. The inner X-ray ring consists of a series of knots that routinely form, brighten, and then dissipate. This behavior is illustrated in Figure 4 which presents HST and Chandra images of the inner Crab region at two different epochs; brightening of wisps to the northwest of the pulsar, as well as knots on the southeastern portion of the inner ring, are particularly evident. In addition, a feature at the base of the pulsar jet (indicated by arrows) is seen to brighten in both the X-ray and optical bands between the two epochs.

*Chandra* observations of PSR B1509–58 also reveal compact knots just outside the pulsar (Figure 2, left), and multi-epoch observations reveal variations in both position and brightness of these knots (Gaensler, 2004). Similarly, structures near PSR J1811-1925 in G11.3–0.3 are observed to brighten and shift in position between two widely-separated observations (Roberts et al., 2003). These features appear to correspond to unstable, quasi-stationary shocks in the region just outside the wind termination shock, where the cold pulsar wind is accelerated and joins the interior of the PWN.

Recent MHD models for PWNe created by anisotropic winds (e.g. Komissarov & Lyubarsky 2004) have had success at reproducing the general jet/toroid structure observed in the Crab and other systems. The termination shock itself is much closer to the pulsar in the polar regions due to the toroidal magnetic field geometry. Additional structure appears to result from a series of shocks, with the position of the observed radiation depending on the geometry of the inner shock region as well as the viewing angle of the observer. In particular, the model of Komissarov & Lyubarsky (2004) is able to reproduce the knot at the base of the Crab jet. However, while this knot is located on the jet side of the pulsar axis, knots observed in PSR B1509–58 are located on the opposite side. This may imply a different viewing geometry, or may suggest that these variable features correspond to a completely different mechanism. Additional study of such dynamic knots are required to address this issue.

Additional complications that remain to be explained and modeled are the curved nature of many pulsar jets as well as the observed intensity variations between jets and counterjets as well as around the toroidal structures. Additional high resolution observations are sure to provide new insights and constraints into such modeling.

#### 4 Filamentary Structure in PWNe

Extensive filamentary structure is observed in  $H\alpha$ , [OIII], and other optical line images of the Crab Nebula. Based on their observed velocities, these fila-

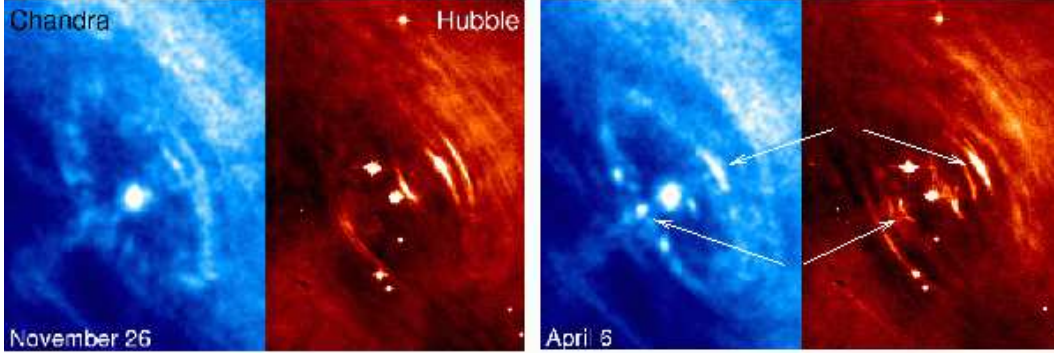


Fig. 4. *Chandra* and HST images of the Crab Pulsar and its surroundings taken at different epochs. The lower arrows in the image at the right indicate compact structures at the base of the jet that have undergone dramatic changes in brightness between the two epochs. The upper arrows indicate regions just outside the wind termination shock that have undergone dramatic changes in brightness.

ments form an expanding shell of ejecta that surrounds the nonthermal optical emission from the nebula. High resolution images with HST reveal detailed morphology and ionization structure suggesting that the filaments form from Rayleigh-Taylor instabilities as the expanding relativistic bubble encounters slower moving ejecta (Hester et al., 1996), a picture supported by MHD simulations that show that 60-75% of the swept-up mass ends up concentrated in such filaments (Jun 1998, Bucciantini et al. 2004). Radio observations reveal filaments that coincide with these optical filaments, presumably corresponding to synchrotron emission from regions of enhanced density and magnetic field in the form of magnetic sheaths that form as the pulsar-injected energy encounters the thermal filaments (Reynolds, 1988). Such filamentary structure is not observed in X-rays, however, suggesting that the electrons with sufficient energy to radiate X-rays do not reach the shell of filaments, or that in situ shock acceleration is not producing them. This is consistent with the observed smaller extent of the X-ray emission in the Crab nebula relative to its radio size, and indicates a larger magnetic field, and thus more rapid synchrotron losses, than is observed in 3C 58 and PSR B1509–58.

Recent *Chandra* observations of 3C 58 reveal a complex of loop-like filaments most prominent near the central regions of the PWN (Figure 3, left), but evident throughout the nebula (Slane et al., 2004). These structures, whose X-ray spectra are nonthermal, are very well correlated with features observed in the radio band (Reynolds and Aller, 1988). Optical observations reveal faint thermal filaments as well (van den Bergh, 1978), which presumably have an origin similar to that of the Crab filaments. The velocities of these optical filaments in 3C 58 are  $\sim \pm 900 \text{ km s}^{-1}$  (Fesen, 1983), sufficiently high to indicate that the PWN is young, but too small to account for the current size of 3C 58 if the historical age is assumed – one of several standing problems with regard to its evolution. A detailed comparison of the X-ray and optical images shows that most of the X-ray filaments do not have corresponding optical

structures, however. While comparisons with deeper optical images are clearly needed, the fact that many of the X-ray features without optical counterparts are brighter than average in X-rays suggests that these may actually arise from a different mechanism. Slane et al. (2004) propose that the bulk of the discrete structures seen in the X-ray and radio images of 3C 58 are magnetic loops torn from the toroidal field by kink instabilities. In the inner nebula, the loop sizes are similar in diameter to the size of the termination shock radius ( $\sim 0.1$  pc), as suggested by Begelman (1998). As the structures expand, they enlarge slightly as a consequence of the decreasing pressure in the nebula. Some of the observed X-ray structure in the outermost regions may be the result of thermal filaments produced by Rayleigh-Taylor instabilities, similar to the filaments in the Crab Nebula. An outer shell of thermal X-ray emission (shown in red in Figure 5) demonstrates the presence of ejecta in these outer regions. While some of the optical filaments do appear to be located in the central regions, these may lie primarily along a shell seen in projection.

We note that considerable loop-like filamentary structure is evident in *Chandra* observations of the Crab Nebula (Weisskopf et al., 2000). These features are primarily observed encircling the bright Crab torus, perpendicular to the toroidal plane, and may result from currents within the torus itself. It is at least conceivable that such currents are signatures of the kink instabilities suggested above.

## 5 Conclusions

High resolution X-ray studies of young pulsars and their associated wind nebulae reveal a broad range of structures that are changing our view on how pulsars interact with their surroundings. The clear evidence of jets and toroidal structures gives a determination of the system geometry as well as physical scales and luminosities for sites of particle acceleration. This, in turn, constrains models for the overall morphology of PWNe as well as for jet confinement, pulsar kicks, and the conversion of the cold pulsar wind into the observed synchrotron nebulae. Filamentary structure provides evidence of the ejecta into which the nebulae are expanding, and also indications of magnetic structures whose nature is currently not well understood. While the Crab pulsar and its nebula have dominated theoretical considerations on PWNe for the past thirty years, current observations are providing a vast amount of information on similarities as well as gross differences between the Crab and other PWNe, offering great promise of dramatically expanding our understanding of these systems.

## Acknowledgments

I would like to thank the many colleagues with whom I have worked on studies of young neutron stars and their wind nebulae for their contributions to my understanding of numerous topics in this field. Special thanks to Okkie de Jager and Rob Petre for their helpful comments in refereeing this paper. This work was supported in part by the National Aeronautics and Space Administration through contract NAS8-39073 and grants GO0-1117A and NAG5-9281.

## References

- Aschenbach, B., Brinkmann, W., 1975. A model of the X-ray structure of the Crab Nebula. *A&A* 41, 147.
- Begelman, M. C., 1998. Instability of Toroidal Magnetic Field in Jets and Plerions. *ApJ* 493, 291.
- Begelman, M. C., Li, Z., 1992. An axisymmetric magnetohydrodynamic model for the Crab pulsar wind bubble. *ApJ* 397, 187–195.
- Bietenholz, M. F., Hester, J. J., Frail, et al. 2004. The Crab Nebula’s Wisps in Radio and Optical. [astro-ph/0408061](https://arxiv.org/abs/astro-ph/0408061).
- Bucciantini, N., Amato, E., Bandiera, R., Blondin, et al. 2004. Magnetic Rayleigh-Taylor instability for Pulsar Wind Nebulae in expanding Supernova Remnants. *A&A* 423, 253–265.
- Camilo, F., Lorimer, D. R., Bhat, N. D. R., et al., 2002. Discovery of a 136 millisecond radio and X-ray pulsar in supernova remnant G54.1+0.3. *ApJ* 574, L71–L74.
- Fesen, R. A., 1983. Discovery of large radial velocities in the supernova remnant 3C 58. *ApJL* 270, L53–L57.
- Frail, D. A., Moffett, D. A., 1993. Deep VLA imaging of pulsar-powered nebulae and the beaming fraction of young pulsars. *ApJ* 408, 637–645.
- Gaensler, B. M., 2004. Shocks and Wind Bubbles Around Energetic Pulsars. [astro-ph/0405290](https://arxiv.org/abs/astro-ph/0405290).
- Gaensler, B. M., Arons, J., Kaspi, V. M., et al., 2002. High-resolution X-ray imaging of pulsar B1509–58 and its environment. *ApJ* 569, 878–893.
- Gallant, Y. A., Arons, J., 1994. Structure of relativistic shocks in pulsar winds: A model of the wisps in the Crab Nebula. *ApJ* 435, 230.
- Greiveldinger, C. and Aschenbach, B. Temporal Variability of the X-Ray Emission of the Crab Nebula Torus. *ApJ* 510, 305–311.
- Helfand, D. J., Gotthelf, E. V., Halpern, J. P., 2001. Vela Pulsar and Its Synchrotron Nebula. *ApJ* 556, 380–391.
- Hester, J. J., 1998. Wind interactions in the Crab Nebula. *Mem. della Soc. Ast. It.* 69, 883.

- Hester, J. J., Mori, K., Burrows, D., et al., 2002. Hubble Space Telescope and Chandra Monitoring of the Crab Synchrotron Nebula. *ApJL* 577, L49–L52.
- Hester, J. J., Stone, J. M., Scowen, P. A., Jun, et al., 1996. WFPC2 Studies of the Crab Nebula. III. Magnetic Rayleigh-Taylor Instabilities and the Origin of the Filaments. *ApJ* 456, 225–233.
- Jun, B., 1998. Interaction of a Pulsar Wind with the Expanding Supernova Remnant. *ApJ* 499, 282.
- Kaspi, V. M., Roberts, M. S. E., Vasisht, G., et al., 2001. Chandra observations of G11.2-0.3: Implications for pulsar ages. *ApJ* 560, 371–377.
- Kennel, C. F., Coroniti, F. V., 1984. Magnetohydrodynamic model of Crab Nebula radiation. *ApJ* 283, 710–730.
- Komissarov, S. S., Lyubarsky, Y. E., 2004. Synchrotron nebulae created by anisotropic magnetized pulsar winds. *MNRAS* 349, 779–792.
- Lai, D., Chernoff, D. F., Cordes, J. M., 2001. Pulsar jets: implications for neutron star kicks and initial spins. *ApJ* 549, 1111–1118.
- Lu, F. J., Wang, Q. D., Aschenbach, B., et al., 2002. Chandra observation of supernova remnant G54.1+0.3: A close cousin of the Crab Nebula. *ApJ* 568, L49–L52.
- Murray, S. S., Slane, P. O., Seward, F. D., et al., 2002. Discovery of X-ray pulsations from the compact central source in the supernova remnant 3C 58. *ApJ* 568, 226–231.
- Ng, C.-Y., Romani, R. W., 2004. Fitting pulsar wind tori. *ApJ* 601, 479–484.
- Pavlov, G. G., Teter, M. A., Kargaltsev, O., Sanwal, D., 2003. The Variable Jet of the Vela Pulsar. *ApJ* 591, 1157–1171.
- Pelling, R. M., Paciesas, W. S., Peterson, L. E., Makishima, K., Oda, M., Ogawara, Y., and Miyamoto, S., 1987. A scanning modulation collimator observation of the high-energy X-ray source in the Crab Nebula. *ApJ*, 319, 416-425.
- Rees, M. J., Gunn, J. E., 1974. The origin of the magnetic field and relativistic particles in the Crab Nebula. *MNRAS* 167, 1–12.
- Reynolds, S. P., 1988. Filamentary structure in Crab-like supernova remnants. *ApJ* 327, 853–858.
- Reynolds, S. P., Aller, H. D., 1988. Radio observations of the Crab-like supernova remnant 3C 58. I - Total intensity observations. *ApJ* 327, 845–852.
- Roberts, M. S. E., Tam, C. R., Kaspi, V. M., et al., 2003. The Pulsar Wind Nebula in G11.2-0.3. *ApJ* 588, 992–1002.
- Romani, R. W., Ng, C.-Y., Mar. 2003. The Pulsar Wind Nebula Torus of PSR J0538+2817 and the Origin of Pulsar Velocities. *ApJL* 585, L41–L44.
- Scargle, J. D., 1969. Activity in the Crab Nebula. *ApJ* 156, 401.
- Slane, P., Helfand, D. J., van der Swaluw, E., et al., 2004. New constraints on the structure and evolution of the pulsar wind nebula 3C 58. *ApJ* 616, 403.
- Slane, P. O., Helfand, D. J., Murray, S. S., 2002. New constraints on neutron star cooling from chandra observations of 3C 58. *ApJ* 571, L45–L49.
- Spitkovsky, A., Arons, J., 2004. Time dependence in relativistic collisionless shocks: Theory of the variable “wisps” in the Crab Nebula. *ApJ* 603, 669–

- 681.
- van den Bergh, S., 1978. Observations of the Optical Remnant of SN 1181 = 3C 58. *ApJL* 220, L9+.
- van der Swaluw, E., Downes, T. P., Keegan, R., 2004. An evolutionary model for pulsar-driven supernova remnants. A hydrodynamical model. *A&A* 420, 937–944.
- Weisskopf, M. C., Hester, J. J., Tennant, A. F., et al., 2000. Discovery of spatial and spectral structure in the X-ray emission from the Crab Nebula. *ApJ* 536, L81–L84.